MEASUREMENT SCIENCE REVIEW, **25**, (2025), No. 6, 347-357

sciendo

ISSN 1335-8871

MEASUREMENT SCIENCE REVIEW

Journal homepage: https://content.sciendo.com

Skin Impedance Analysis for Drug Delivery: Integration of Poisson–Boltzmann–Nernst–Planck Model and Ebola Optimisation Algorithm

Maceal Tony L[1*], Shaji R.S[2]

[1]*Department of Electronics and Communication Engineering, St. Xavier's Catholic College of Engineering, Nagercoil, India, maceal@sxcce.edu.in*
[2]*Department of Computer Science and Engineering, St. Xavier's Catholic College of Engineering, Nagercoil, India, shaji@sxcce.edu.in*

Abstract: Transdermal drug delivery (TDD) is a non-invasive approach for administering therapeutic medications through the skin. This research proposes a spine–leaf resistor–capacitor (SLRC) circuit to analyse the impedance characteristics of different skin layers during drug delivery. To optimise the SLRC circuit parameters, the Ebola Optimisation Algorithm (EOA) minimises errors and improves computational efficiency. The Poisson–Boltzmann–Nernst–Planck (PBNP) model is used to calculate input parameters such as ion concentrations and electrotransport flux, to derive the drug concentration based on input parameters. A MATLAB simulator calculates drug penetration across stratified skin regions. According to the SLRC results, the Montague, constant phase element (CPE), and Tregear models performed better in predicting drug penetration and electrotransport flux than more conventional models. Compared to the traditional Montague and Tregear models, the EOA improved performance by reducing the mean absolute percentage error (*MAPE*) to as low as 0.134. The proposed model achieved an R^2 value of 0.98 when validated against the impedance datasets, confirming high prediction accuracy. Furthermore, simulated results revealed that an optimal frequency of 4×10^3 Hz provides the best impedance and drug penetration, demonstrating the importance of frequency and current density in increasing drug levels. The proposed model enhances the precision and efficiency of TDD, offering significant potential for clinical and pharmaceutical applications.

Keywords: transdermal drug delivery, iontophoresis, spine–leaf resistor–capacitor, Ebola Optimisation Algorithm, Poisson–Boltzmann–Nernst–Planck

1. INTRODUCTION

In medical history, traditional drug administration methods include oral ingestion and hypodermic injections [1]. Transdermal drug delivery (TDD) is a technique for delivering medications through the skin [2], [3]. TDD is an innovative and non-invasive method of administering therapeutic agents through the skin to achieve systemic effects [4], [5]. TDD systems, such as patches, gels, and creams, offer significant benefits over traditional delivery techniques, including improved patient compliance, controlled drug release, and fewer adverse effects [6], [7]. TDD continues to evolve with advancements in nanotechnology, microneedles, and permeation enhancers, broadening its potential applications in modern medicine [8].

Iontophoresis is a non-invasive technique used to transport ions and charged molecules across skin membranes using a low-level electrical current [9], [10]. Iontophoresis-based sweat testing for diseases such as cystic fibrosis is also used in research and diagnostics [11]. The intricate features of human skin must be considered when administering transdermal drugs [12], [13]. The skin contains keratinised cells, sweat glands, hair follicles, and pores [14]. Skin impedance as a key component of bioimpedance has been used to analyse various data about underlying tissues, including fat deposits, moisture content, and other relevant factors [15].

The Nernst–Planck (NP) model [16] describes the transport of ions under both concentration gradients and electric fields. It considers both diffusion (due to concentration gradients) and migration (due to the electric field).

$$J_\tau = -D_\tau \nabla n_\tau - \frac{z_\tau F}{RT} n_\tau \nabla \varphi \tag{1}$$

where J_τ represents the ion flux, D_τ is the diffusion coefficient of the ion species, τ is a general index for ion species used to define ion-specific properties such as diffusion and charge, n_τ is the concentration of the ion species, z_τ is the valence of τ, F is Faraday's constant, R is the universal gas constant, T is temperature, φ is the electric potential, and ∇ is the gradient operator.

DOI: 10.2478/msr-2025-0038

Corresponding author: maceal@sxcce.edu.in (Maceal Tony L)

The Poisson–Nernst–Planck (PNP) model [17] extends the NP model by incorporating the Poisson equation to account for the electrostatic potential distribution within the system, which depends on the charge distribution. The Poisson equation for the electrostatic potential φ is given by,

$$\nabla^2\varphi = -\frac{\rho}{\epsilon} \tag{2}$$

where ρ is the charge density and ϵ is the permittivity of the medium. The PNP model integrates the Poisson equation to solve for the electrostatic potential φ, which is influenced by the ion distribution. To address this challenge, the PNP model can be reformulated to reduce computational overhead by representing certain ion species differently. In this alternative model, let n denote the total number of ion species. The target ion species are denoted as $n_{\propto}(\propto= 1,2,3, \dots N_{NP})$, where N_{NP} is the number of ions treated using the NP equation. The remaining ions, denoted $n_{\beta}(\beta = N_{NP} + 1, \dots, N_c)$, are modelled using the Boltzmann distribution. Here, $n_{\propto}$ represents the number of target ion species modelled using the Nernst–Planck equations, and n_{β} represents the number of non-target ion species modelled using the Boltzmann distribution. The index $\propto$ denotes the index for target ions modelled via the NP equations, while β denotes the index for non-target ions modelled via the Boltzmann distribution.

Several researchers have proposed electrically equivalent models of the skin to account for its dynamic physiological stratification. The most commonly used techniques, such as the Tregear model [18] and the Montague model [19], classify the skin as a resistor–capacitor (RC) layered system. The transfer functions of three electrical models of human skin (Montague, Tregear, and Lykken models) were analysed in terms of physical stratification [20]. A nanomaterial-based TDD platform using a nucleic acid framework [26] was developed for enhanced photodamage treatment. The results demonstrated high drug-loading efficiency and controlled release via UV activation. Optical coherence tomography (OCT) and fluorescence imaging [27] were employed to visualise microneedle-assisted drug diffusion, enabling real-time tracking of drug delivery depth and efficiency with high spatial resolution. A wearable device was designed [28] for continuous skin impedance spectroscopy under real-time conditions, focusing on conductivity changes over time. Moreover, the impedance changes in pig skin were investigated using tape stripping [29] to remove layers and measure electrical responses. However, experimental validation of impedance variability across skin layers lacks computational optimisation and electrotransport modelling. This research introduces a systematic approach to device-assisted transdermal drug delivery by integrating physical modelling and mathematical frameworks to predict drug concentration across skin layers. The key contributions of the proposed work are summarised as follows:

- A novel spine–leaf resistor–capacitor (SLRC) circuit is introduced, combining the Montague, constant phase element (CPE), and Tregear models to more accurately simulate skin impedance across various stratified layers.
- The PBNP model is incorporated to achieve precise calculation of ion transport and drug flux under electric fields, improving the predictive modelling of TDD.
- The Ebola Optimisation Algorithm (EOA) is used to optimise the SLRC circuit parameters, significantly reducing the computational error and improving prediction accuracy.
- The proposed model is validated across 12 different human body regions, revealing the impact of biophysical skin properties on drug delivery efficiency, which provides valuable insights for clinical settings.

The rest of the paper is organised as follows: Section 2 provides a comprehensive description of the proposed framework for analysing drug penetration across various skin layers; Section 3 presents the results and comparison of the proposed framework; Section 4 discusses the comprehensive validation of five different circuits; and finally, Section 5 concludes with a summary and future work.

2. MATERIALS AND METHODS

In this section, we present a systematic approach to device-assisted TDD by integrating advanced modelling techniques and an optimisation algorithm. The SLRC circuit is introduced to analyse the impedance characteristics of different skin layers during drug delivery. The PBNP model enables precise calculation of electrotransport flux and drug concentrations across various skin layers by improving the predictive performance of drug delivery systems. The overall workflow of the proposed methodology is shown in Fig. 1.

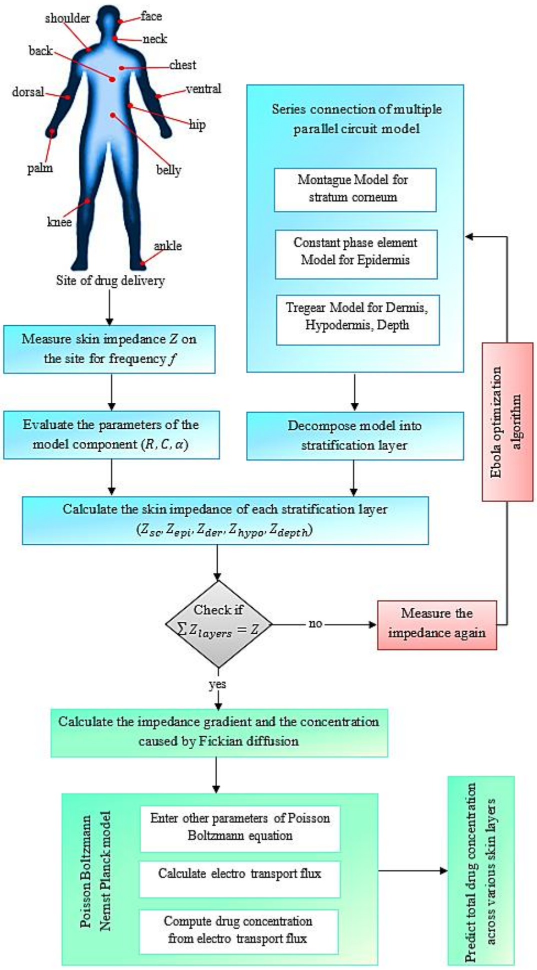

Fig. 1. Sequence of steps adopted in this research for drug delivery.

A. Series connection of multiple parallel circuit models

In this work, the SLRC circuit is introduced with a series connection of multiple parallel circuits. The SLRC circuit combines the Montage, CPE, and Tregear models for five different skin layers, as shown in Fig. 2. These models were developed based on physiological stratification and the chemical and biological characteristics of the skin. A series of skin impedance models was examined in this research. The flowchart of the proposed work for predicting drug penetration across various skin layers is shown in Fig. 3.

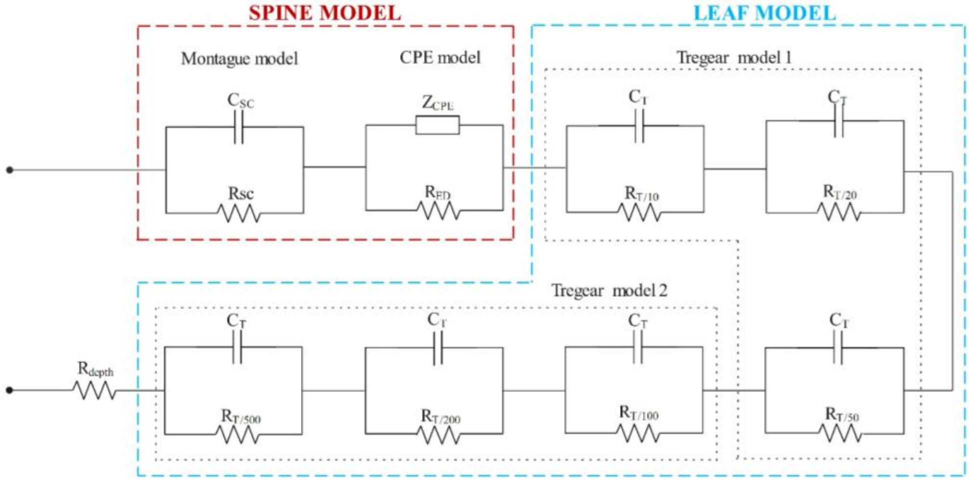

Fig. 2. Spine–leaf resistor–capacitor circuit.

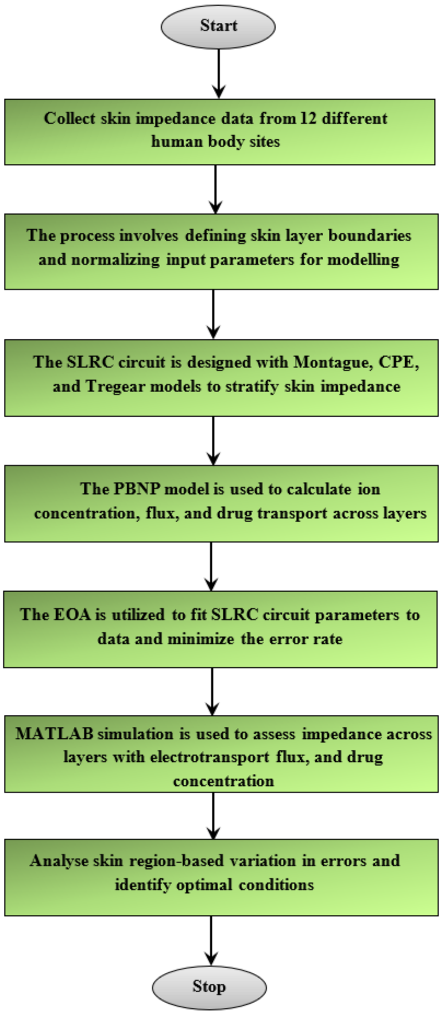

Fig. 3. Flowchart of the proposed model for predicting drug penetration across various skin layers.

Montague model

The Montague model [21] is the simplest and most common model for skin stratification based on physiological factors. In this model, the properties of the resistor and capacitor for the stratum corneum (SC) are represented in parallel by a resistive R_{sc} and a dielectric capacitance C_{sc}. Skin resistance is represented by a small resistance R_s, which is connected in series with this parallel combination. The impedance function associated with this model is given by,

$$G(S) = \frac{R_{\mathrm{sc}} + R_{\mathrm{s}} + sR_{\mathrm{sc}}R_{\mathrm{s}}C_{\mathrm{sc}}}{sR_{\mathrm{sc}}R_{\mathrm{s}}C_{\mathrm{sc}} + 1} \tag{3}$$

where R_{sc} represents the resistance of the SC, indicating the outermost skin layer's resistance to electric current. R_{s} denotes the small resistance of the skin's deeper layers, connected in series. C_{sc} represents the dielectric capacitance of the SC, modelling the SC's ability to store electrical energy as a dielectric material. Here, s is the Laplace transform variable associated with frequency in the impedance function, describing the dynamic behaviour of the system.

Constant phase element (CPE) model

The CPE model [22] is widely used in electrical impedance analysis to describe non-ideal capacitive behaviour. The Montague model uses a CPE instead of an ideal capacitor. The impedance of the CPE is represented as Z_{cpe}. In a quasi-capacitor, the impedance A represents the impedance. In terms of fractal dimensions, the most significant dimension on the surface of the skin is α. A CPE acts as a pure capacitor, resistor, and inductor at $\alpha = 1, 0,$ and -1, respectively. A fractional CPE forms the basis for this model, which is called the CPE-based model for capturing the genetic properties of skin. Equation (3) represents the relevant impedance function for the CPE model:

$$G(S) = R_s + \frac{R_{\mathrm{ED}}}{1 + R_{\mathrm{ED}} A s^{\alpha}} \tag{4}$$

where R_{ED} represents the resistance of the epidermis, and α is a fractional exponent ($0 \leq \alpha \leq 1$) indicating the degree of non-ideal capacitive behaviour, with $\alpha = 1$ for ideal and lower values for more distributed responses.

Tregear model

The Montague model [23] comprises three fixed component values. Skin impedance values change as we move deeper into the skin layers from the surface. In these situations, the Montague model does not account for changes in impedance due to the physiological stratification of the skin. Because of this limitation, the Montague model is prone to flaws and errors. In this study, Tregear and colleagues found that tape stripping reduces the impedance value with each strip. Tregear constructed several parallel RC circuits in series to illustrate the varying resistance and capacitance values across different skin layers.

The Tregear model consists of three levels (each with resistance (R_{T}) and capacitance (C_{T})). As levels increase, deeper layers of skin are considered. Level 3 of the Tregear model is the highest level that can be considered. The model therefore accounts for the skin's physiological stratification at a very deep level. In (5) and (6), we present the corresponding impedance functions for Level 1 and Level 2 of the Tregear model.

$$G(S) = \frac{R_{\mathrm{T}}}{sR_{\mathrm{T}}C_{\mathrm{T}} + 1} + \frac{R_{\mathrm{T}}}{sR_{\mathrm{T}}C_{\mathrm{T}} + 2} + \frac{R_{\mathrm{T}}}{sR_{\mathrm{T}}C_{\mathrm{T}} + 5} \tag{5}$$

$$\begin{aligned} G(S) = {} & \frac{R_{\mathrm{T}}}{sR_{\mathrm{T}}C_{\mathrm{T}} + 1} + \frac{R_{\mathrm{T}}}{sR_{\mathrm{T}}C_{\mathrm{T}} + 2} + \frac{R_{\mathrm{T}}}{sR_{\mathrm{T}}C_{\mathrm{T}} + 5} \\ & + \frac{R_{\mathrm{T}}}{sR_{\mathrm{T}}C_{\mathrm{T}} + 10} + \frac{R_{\mathrm{T}}}{sR_{\mathrm{T}}C_{\mathrm{T}} + 20} + \frac{R_{\mathrm{T}}}{sR_{\mathrm{T}}C_{\mathrm{T}} + 50} \end{aligned} \tag{6}$$

Hybrid model

The proposed Spine leaf model represents both the biological characteristics and physiological stratification of skin. A parallel combination of a resistor (R_{sc}) and CPE (R_{ED}) represents the combined impedance of the SC and epidermis. Three parallel combinations of different resistors (R_{T}) and a capacitor (C_{T}) represents the various layers of the dermis, hypodermis, and depth layers. The resistance of the deepest layer is denoted by a low-value resistor, R_{depth}. The values are ($R_{\mathrm{T}} = R_{\mathrm{SC}}$) Ω, ($C_{\mathrm{T}} = A$), and $R_{\mathrm{depth}} = 200\ \Omega$. Equation (7) gives the equivalent impedance function for the hybrid model.

$$\begin{aligned} G(S) = {} & \frac{R_{\mathrm{SC}}}{sR_{\mathrm{SC}}C_{\mathrm{SC}} + 1} + \frac{R_{\mathrm{ED}}}{R_{\mathrm{ED}} A s^{\alpha} + 1} + \frac{R_{\mathrm{T}}}{sR_{\mathrm{T}}C_{\mathrm{T}} + 10} \\ & + \frac{R_{\mathrm{T}}}{sR_{\mathrm{T}}C_{\mathrm{T}} + 20} + \frac{R_{\mathrm{T}}}{sR_{\mathrm{T}}C_{\mathrm{T}} + 50} + \frac{R_{\mathrm{T}}}{sR_{\mathrm{T}}C_{\mathrm{T}} + 100} \\ & + \frac{R_{\mathrm{T}}}{sR_{\mathrm{T}}C_{\mathrm{T}} + 200} + \frac{R_{\mathrm{T}}}{sR_{\mathrm{T}}C_{\mathrm{T}} + 500} + R_{\mathrm{depth}} \end{aligned} \tag{7}$$

In the SLRC circuit, the capacitive component primarily represents the restriction of ion transport across the SC layer. For model fitting, resistance values are set between 0.1 and 100 kΩ and capacitance values between 0.01 and 10 nF. In MATLAB, the Levenberg–Marquardt algorithm was configured with 200 iterations and 1e^{-6} convergence tolerance as one of the solver settings. To further optimise the circuit parameters, the EOA was used with a population size and maximum number of iterations selected via grid search for optimal performance.

B. Ebola search Optimisation Algorithm

In this section, the parameters of the proposed SLRC circuit are obtained from the impedance dataset using a non-linear least squares fitting in MATLAB. The EOA [24] is applied to optimise the simulated parameters to fit into the collected dataset, as shown in Fig. 4. EOA is a nature-inspired metaheuristic optimisation technique modelled after the propagation dynamics of the Ebola virus. In the context of the proposed SLRC circuit, EOA is used to optimise simulated circuit parameters (such as resistance *R* and capacitance *C*) to fit experimental data or a collected dataset. The EOA addresses the limited optimisation problem through the following steps:

- Evaluate the effectiveness of iontophoresis by analysing the current density, drug concentration, and duration influence on skin permeability and drug absorption.
- If a parameter set does not meet safety thresholds or if skin penetration is less than ideal, discard it.
- Combine and modify parameters from the sets that work well, ensuring a balance between safety and efficacy, to improve iontophoresis outcomes.
- Repeat the first step and adjust the settings until the ideal conditions or the convergence criteria (such as negligible performance improvement or a safety issue) are met.

The formula for the skin impedance of the SLRC circuit is derived as

$$Z = \sqrt{R^2 + \left({}^{1}\!/_{\omega C}\right)^2} \tag{8}$$

where Z represents the skin impedance of the SLRC circuit and ω is the angular frequency of the circuit. Substitute $\omega = 2\pi f$ into the above equation (8)

$$Z = \sqrt{R^2 + \left({}^{1}\!/_{2\pi f C}\right)^2} \tag{9}$$

Square both sides to eliminate the square root

$$Z^2 = R^2 + \left({}^{1}\!/_{2\pi f C}\right)^2 \tag{10}$$

Invert the equation (10)

$$2\pi f C = {}^{1}\!/_{\sqrt{Z^2 - R^2}} \tag{11}$$

$$f = {}^{1}\!/_{2\pi C\sqrt{Z^2 - R^2}} \tag{12}$$

This EOA determines the parameter values with the lowest $f - value$. The EOA parameters initialise a population size of 50, and an iteration count of 200 is selected based on grid search tuning for biomedical optimisation tasks. The initial grid search tuning was performed by varying the population size (30-70) and iterations (100-300) to evaluate the convergence speed and error minimisation. The selected configuration (i.e., size = 50, iteration = 200) provided the optimal trade-off between prediction accuracy and a low error rate. As a result, this setup ensures consistent efficiency while maintaining modest processing requirements for drug delivery studies based on simulation.

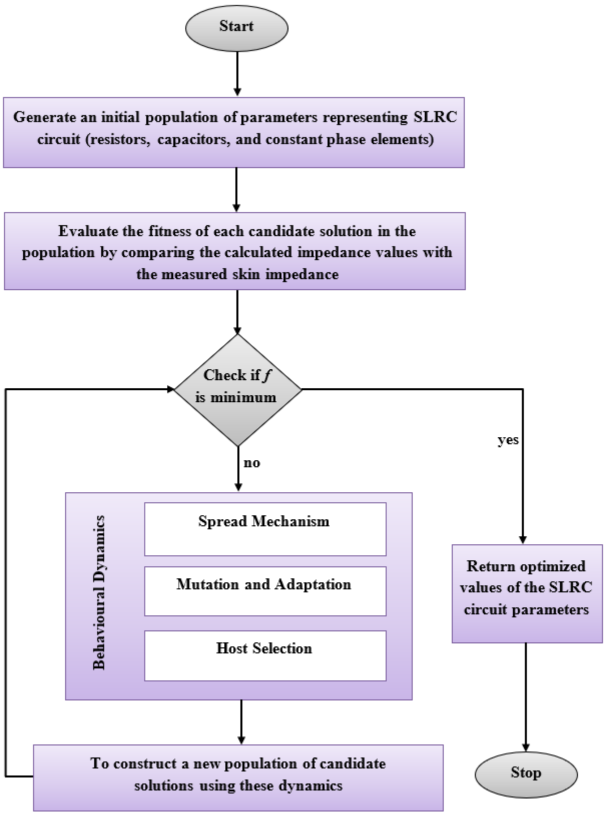

Fig. 4. Flowchart of the Ebola Optimisation Algorithm for SLRC circuit parameter normalisation.

In the EOA, parameter values are passed to an objective function, which aims to produce a result indicating the parameters are "good". Fitting datasets Z_{fit} are created based on the parameters that provide the best fit for a given model. The mean absolute percentage error ($MAPE$) measures the statistical predictive performance of the proposed method. It usually conveys accuracy through (13):

$$MAPE = \frac{1}{n}\sum_{i=1}^{n} \left| \frac{(Z_{\text{fit}} - A_{\text{data}})}{A_{\text{data}}} \right| \tag{13}$$

where n is the number of fitting points, Z_{fit} is the predicted value from the circuit, and A_{data} is the actual observed value. A model with a low $MAPE$ value produces the best results. Calculating fitness accuracy involves calculating the coefficient of determination (R^2). This provides insight into the goodness of fit of a model in statistics, and it measures the accuracy of regression predictions by comparing them to the actual data points.

C. *Poisson–Boltzmann–Nernst–Planck model*

The PBNP model [25] extends the PNP model by incorporating Boltzmann distributions to account for equilibrium ion concentrations under potential fields. The PBNP model is formulated as a hybrid approach to efficiently simulate ion transport in multi-layered skin under iontophoretic stimulation. Specifically, this hybrid approach integrates the NP equation for target ion-species and the Boltzmann distribution for non-target ions. Target ions are assumed to undergo active electro-diffusion, while non-target ions are assumed to be in quasi-equilibrium, reducing computational complexity without compromising accuracy. Boundary conditions include a fixed potential (Dirichlet) at the skin surface and zero-ion flux (Neumann) at the deepest boundary. Continuity conditions are enforced for ion flux and potential at layer interfaces.

Multi-ionic systems such as cutaneous medication administration, particularly benefit from this method because they involve interactions between ions and an electric field. The Boltzmann distribution for ion concentration is given by:

$$n_\tau = n_\tau^0 \exp\left(-\frac{z_\tau F \varphi}{RT}\right) \tag{14}$$

The derived flux equation for the PBNP model is:

$$J_\tau = \frac{D_\tau z_\tau F n_\tau}{RT} I \frac{\mathrm{d}z}{\mathrm{d}x} \tag{15}$$

This model provides a comprehensive understanding of how ions and medications permeate through skin layers under an electric field, aiding the advancement of iontophoretic drug delivery techniques. As a result, it is possible to assess the impedance of the skin at various layers.

3. EXPERIMENTAL RESULTS

In this section, the mathematical solutions of the PBNP model were simulated using MATLAB 2018a to evaluate ion transport and drug diffusion across stratified skin layers. The simulation results presented in this research are supported by in-silico validation using established skin impedance datasets and numerical modelling techniques. The proposed model was evaluated across 12 anatomical regions. The iontophoresis of Naltrexone HCl was simulated using drug and concentration data. Its concentration in dissociated saturated solution at 36 °C (309 K) and its diffusion coefficient are 83.76 × 102 mm^2/s, respectively, after which a dispersed saturated solution of the medication is released from the reservoir. According to our measurements, the concentration of the drug solution was 31.252 g/mm^3. As impedance data were available, iontophoretic drug administration at the 12 different sites of the human body was considered in this investigation. Skin layer thicknesses were 40 mm for SC, 164 mm for the epidermis, 5888 mm for the dermis, 191 mm for the hypodermis, and 2845 mm for depth. The boundaries between the layers were 0, 0.040, 0.164, 6.052, 7.965, and 10 mm, respectively. It is possible to simulate drug diffusion and flux measurements accurately by modelling parameters using impedance data at different kHz.

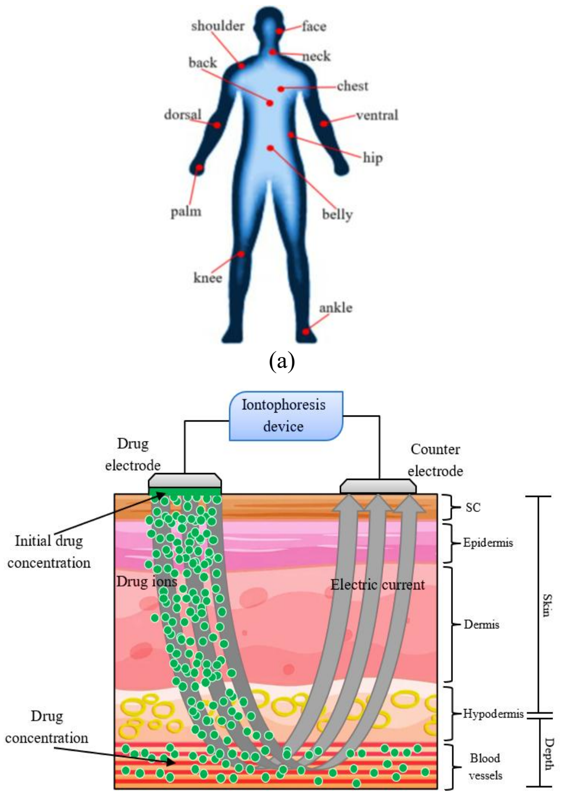

(a)

(b)

Fig. 5. Visual representation of (a) Anatomical sites on the human body considered for iontophoretic drug delivery simulation. (b) Simulated drug concentration profiles across skin depths using the proposed model.

Fig. 5 illustrates the process of TDD using iontophoresis at various skin depths in different sites of the human body. PBNP regulates iontophoretic flux, involving passive diffusion and electrotransport. Drug molecules are delivered through stratified skin layers, with counter electrodes ensuring current flow. Drug concentration diminishes with increasing depth, highlighting the importance of electrical control for targeted delivery.

Table 1 presents the impedance values measured across different skin layers (SC, Epidermis, Dermis, Hypodermis, and Depth) for five models: Montague, CPE, Tregear-1, Tregear-2, and Hybrid. Impedance is highest in the SC and decreases progressively through the deeper layers. The Tregear model shows significant impedance variability across layers.

Table 2 shows electrotransport flux values for each skin layer across the same five models. The flux values are highest in the SC and Epidermis, reflecting their greater transport potential. The deeper layers, such as the Dermis and Hypodermis, show reduced flux due to resistance. Depth exhibits negligible or zero flux in certain models.

Table 3 provides drug concentrations in molar units, highlighting the distribution across skin layers for the models. The SC and Epidermis maintain the highest molar concentrations, consistent with their greater retention capacity. Deeper layers display lower concentrations, while the tissue layer holds the least. The proposed model achieves a more balanced drug distribution across layers.

Table 1. Impedance [Ω cm^2] across different skin layers for all models.

Layer	Montague	CPE	Tregear-1	Tregear-2	SLRC (proposed)
SC	8452.34	8339.12	8210.89	6543.78	6520.43
Epidermis	6295.12	6203.98	6289.67	5082.34	4752.89
Dermis	783.12	710.45	735.56	850.92	903.78
Hypodermis	365.45	285.67	299.45	522.34	610.12
Depth	8.21	0.12	0.00	276.45	371.54

Table 2. Electrotransport flux [µg/mm^{2}s] across different skin layers for all models.

Layer	Montague	CPE	Tregear-1	Tregear-2	SLRC (proposed)
SC	167.12	162.34	165.45	139.87	126.78
Epidermis	125.87	122.76	123.56	103.45	95.34
Dermis	17.12	15.78	16.45	18.12	17.89
Hypodermis	7.12	6.45	6.89	11.34	13.56
Depth	0.34	0.00	0.12	5.87	7.34

Table 3. Total drug concentration [mole/m^3] across different skin layers for all models.

Layer	Montague	CPE	Tregear-1	Tregear-2	SLRC (proposed)
SC	390.67	387.12	392.34	418.12	378.56
Epidermis	328.45	324.67	326.12	275.67	260.78
Dermis	7.12	6.89	7.34	6.12	7.45
Hypodermis	3.89	2.87	3.23	4.45	5.34
Depth	0.65	0.00	0.12	1.78	2.56

In Fig. 6, the Montague model, computational fluid dynamics (CFD)-based model, Tregear 1&2 models, and the Proposed model are among the models used to analyse variations in parameters associated with drug delivery through skin depth. In Fig. 6(a), skin impedance decreases with increasing skin depth, which is crucial for assessing drug penetration. Fig. 6(b) shows a decrease in electrotransport flux across deeper epidermal layers as epidermal depth increases. Fig. 6(c) shows that medication concentration, as determined by the electrotransport mechanism, decreases with greater skin penetration. Due to their consistent trends, these models provide reliable forecasting of drug delivery performance.

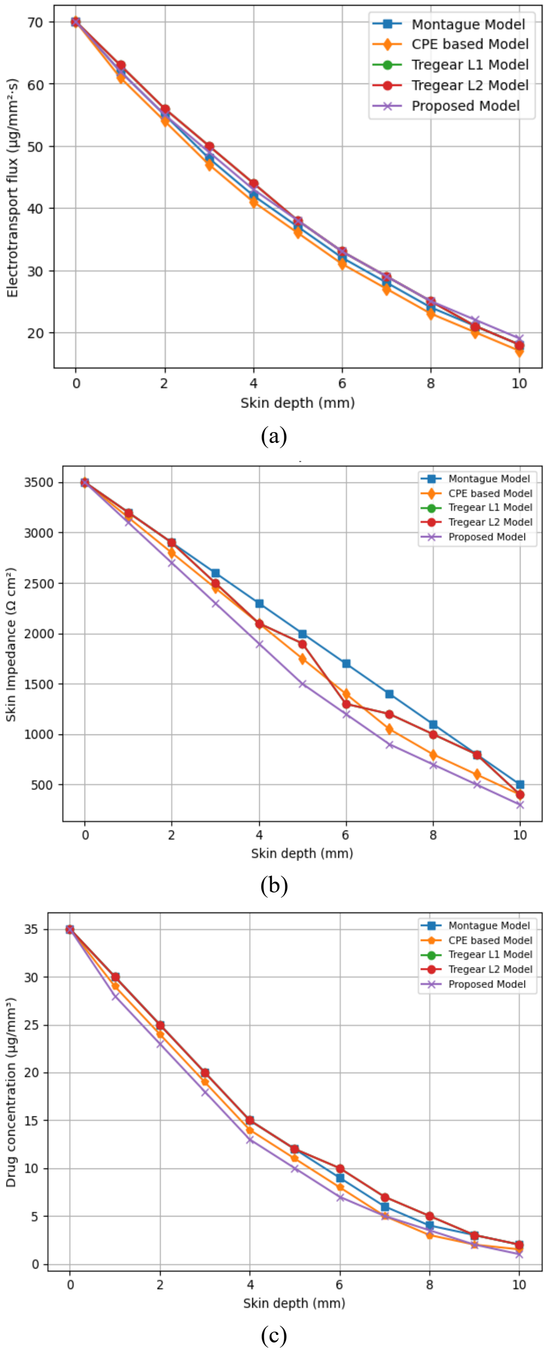

(a)

(b)

(c)

Fig. 6 (a) Skin impedance; (b) Electrotransport flux; and (c) Drug concentration derived from the electrotransport component with variation in skin depth.

Table 4 presents the total drug concentration (mole/m³) across various skin layers at different current densities (*I*, mA/cm²). As current density increases, a significant rise in drug concentration is observed across all layers. The SC shows the highest concentration due to its proximity to the drug source, while the tissue shows the lowest. This trend highlights the direct relationship between current density and drug delivery efficiency during iontophoretic administration.

Table 4. Total drug concentration [mole/m³] with variations in current density (*I*, mA/cm²).

I [mA/cm²]	*I* = 0.1	*I* = 0.2	*I* = 0.4	*I* = 0.5	*I* = 1.0
SC	140.12	205.36	329.85	392.47	710.29
Epidermis	89.34	132.19	218.76	261.42	480.14
Dermis	2.32	3.76	6.45	7.84	15.08
Hypodermis	1.63	2.42	3.89	4.51	8.12
Depth	1.24	1.62	2.36	2.72	4.51

Fig. 7 shows the distribution of drug concentration (μg/mm³) across different skin depths (0-10 mm) under varying current densities (0.1, 0.2, 0.4, 0.5, and 1.0 mA/cm²). Higher current densities result in deeper drug penetration but lower concentrations at the surface. The colour gradient indicates drug concentration, with yellow representing higher values and purple representing lower values. Drug concentration decreases as skin depth increases for all current densities. This highlights the effect of current density on drug delivery efficiency and depth of penetration.

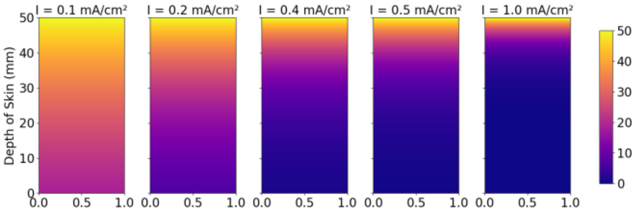

Fig. 7. Total drug concentration [μg/mm³] at different skin layers in current density [mA/cm²].

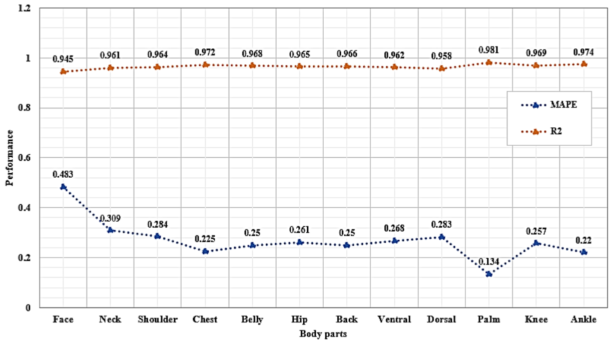

Fig. 8. Analysis of the proposed model based on *MAPE* and R^2 values across various body regions.

Fig. 8 shows the prediction performance of the proposed model across 12 anatomical areas, based on *MAPE* and R^2. According to the table, the palm region has the lowest *MAPE* (0.134) and the highest R^2 (0.981). Each location shows high R^2 values (0.94), indicating a superior model fit across a range of skin types and anatomical variations. Based on these results, the proposed model is versatile and robust enough to optimise medicine administration in specific regions for simulating TDD.

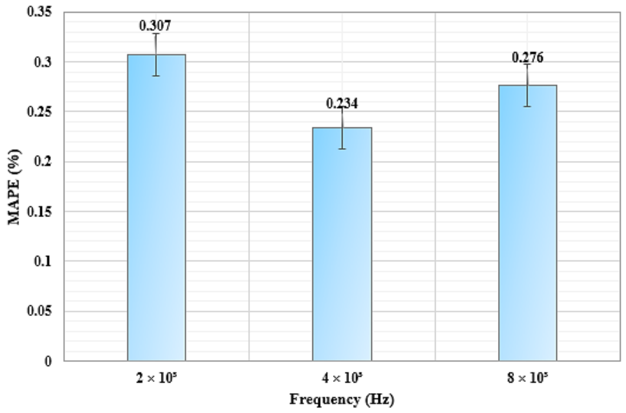

Fig. 9. Performance analysis of the proposed model based on *MAPE* vs Frequency for TDD.

Fig. 9 shows the impact of current frequency on prediction accuracy using *MAPE* as the evaluation metric. Among the tested frequencies, 4 × 10³ Hz produced the lowest *MAPE* (0.234 %), indicating optimal conditions for drug penetration. The reported *MAPE* values at 2 × 10³ Hz and 8 × 10³ Hz were higher, indicating inferior impedance behaviour. This demonstrates the importance of frequency tuning for effective transdermal drug delivery.

Table 5 compares the *mean* and standard deviation (*SD*) of drug delivery efficiency across different body parts at frequencies of 2 × 10³ Hz, 4 × 10³ Hz, and 8 × 10³ Hz. The values show that 4 × 10³ Hz consistently yields lower *mean* values than the other frequencies, indicating optimal conditions for drug delivery. The *SD*s for 4 × 10³ Hz suggest better control and homogeneity of delivery. Compared to 2 × 10³ Hz and 8 × 10³ Hz, higher *mean* values indicate greater resistance and less effective drug penetration. The *SD* for 4 × 10³ Hz is moderate, ensuring controlled delivery with minimal variability compared to other frequencies. All body components exhibit the same pattern, highlighting the higher efficiency of 4 × 10³ Hz. This demonstrates that 4 × 10³ Hz is the most effective frequency for skin medication delivery applications.

Table 5. *Mean* and *SD* [Ω] of impedance for various body parts.

	2 × 10³ Hz		4 × 10³ Hz		8 × 10³ Hz	
Body parts	*Mean*	*SD*	*Mean*	*SD*	*Mean*	*SD*
Face	5.60 × 10³	1840.12	4.20 × 10³	1450.25	6.80 × 10³	2115.37
Neck	1.02 × 10⁴	2155.20	7.85 × 10³	1780.55	1.12 × 10⁴	2401.28
Shoulder	1.10 × 10⁴	2250.30	8.20 × 10³	1720.45	1.18 × 10⁴	2435.12
Chest	1.25 × 10⁴	2445.41	9.05 × 10³	1865.33	1.34 × 10⁴	2560.11
Belly	1.30 × 10⁴	2235.75	9.50 × 10³	1900.25	1.38 × 10⁴	2710.32
Hip	1.18 × 10⁴	2145.88	8.70 × 10³	1805.40	1.26 × 10⁴	2605.45
Back	1.12 × 10⁴	2140.82	8.50 × 10³	1775.55	1.22 × 10⁴	2525.87
Ventral	1.25 × 10⁴	2195.65	9.20 × 10³	1825.75	1.32 × 10⁴	2650.20
Dorsal	1.50 × 10⁴	2280.34	1.05 × 10⁴	1950.45	1.60 × 10⁴	2755.30
Palm	1.75 × 10⁴	2370.12	1.20 × 10⁴	2050.50	1.85 × 10⁴	2855.20
Knee	1.45 × 10⁴	2200.55	1.00 × 10⁴	1850.15	1.55 × 10⁴	2705.75
Ankle	1.60 × 10⁴	2335.22	1.12 × 10⁴	1955.40	1.70 × 10⁴	2800.35

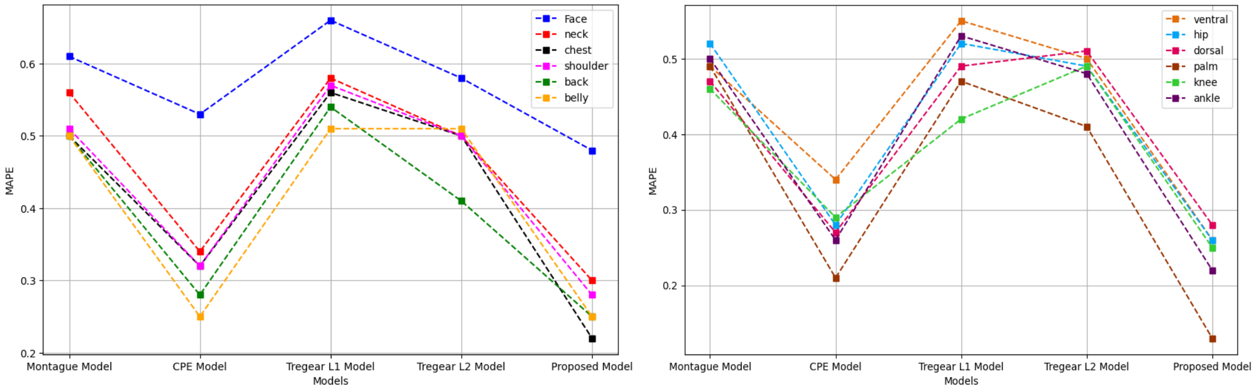

(a) (b)

Fig. 10. *MAPE* value comparison of different models for different body parts (a) Upper body regions and (b) Lower body regions.

Fig. 10 presents a comparative analysis of the proposed model with the Montague model, CPE model, Tregear L1 model, and Tregear L2 model based on *MAPE* values. *MAPE* values for the face, neck, chest, shoulder, back, and belly are shown in Fig.10(a), while ventral, hip, dorsal, palm, knee, and ankle *MAPE* trends are shown in Fig. 10(b). The lower *MAPE* across all body sections indicates superior performance of the proposed model. The CPE model also performs well, especially when it comes to minimising errors. The Montague models show a higher error rate, while the Tregear models provide moderate *MAPE* values. These patterns demonstrate that the proposed model is effective in optimising drug distribution to different parts of the body.

Table 6. Comparison analysis of the proposed SLRC circuit with existing models across various body parts.

	$MAPE$ values					R_{sc}	C_T	S_F	R^2
Body parts	Montague	CPE	Tregear-1	Tregear-2	Proposed	Proposed	Proposed	Proposed	Proposed
Face	0.613	0.531	0.665	0.582	0.483	72.476	0.495	1.000	0.945
Neck	0.561	0.342	0.585	0.506	0.309	17.465	0.496	0.924	0.961
Shoulder	0.518	0.320	0.578	0.501	0.284	13.584	0.451	0.870	0.964
Chest	0.501	0.320	0.564	0.507	0.225	10.027	0.447	0.884	0.972
Belly	0.505	0.256	0.515	0.519	0.250	45.268	0.312	0.998	0.968
Hip	0.520	0.280	0.528	0.498	0.261	38.923	0.315	0.962	0.965
Back	0.505	0.284	0.546	0.415	0.250	15.385	0.286	0.984	0.966
Ventral	0.494	0.343	0.556	0.506	0.268	23.948	0.471	0.908	0.962
Dorsal	0.475	0.272	0.495	0.512	0.283	80.638	0.352	1.000	0.958
Palm	0.494	0.211	0.472	0.418	0.134	18.225	0.441	0.844	0.981
Knee	0.463	0.297	0.424	0.495	0.257	55.687	0.346	0.975	0.969
Ankle	0.505	0.266	0.532	0.483	0.220	40.315	0.417	0.903	0.974

Table 6 presents a performance comparison of the proposed SLRC circuit with existing models across various body parts based on different parameters. These parameters include $MAPE$, skin resistance (R_{sc} in kΩ), capacitance (C_T) in nF), a scaling factor (S_F), and the highest coefficient of determination (R^2). For the palm, the proposed SLRC circuit has a $MAPE$ value of 0.134, where lower values indicate higher prediction accuracy. Skin resistance (R_{sc}) varies between body parts, with the dorsal region (80.636 kΩ) showing the highest value and the chest (10.027 kΩ) the lowest. In the neck, capacitance (C_T) is comparatively constant at 0.499 nF, while it is as low as 0.286 nF in the back. According to Table 7, the SF values across all body parts indicate consistent performance of the proposed model in predicting skin characteristics, providing accurate guidance for optimising transdermal drug delivery strategies. The palm region shows the lowest $MAPE$ (0.134) and the highest R^2 (0.981). Each location shows high R^2 values (0.94), indicating superior model fit across a range of skin types and anatomical variations. Based on these results, the proposed model is versatile and robust enough to optimise medicine administration in specific regions for simulating TDD.

Table 7. Comparison of different optimisation algorithms

Algorithm	$MAPE$	R^2	Convergence time [s]
BO	0.307	0.961	18.6
PSO	0.276	0.948	14.1
GA	0.265	0.954	12.5
EOA (ours)	0.234	0.982	9.3

Table 7 compares existing algorithms such as Bayesian optimisation (BO), particle swarm optimisation (PSO), and genetic algorithm (GA) with the proposed EOA. The EOA achieved the lowest $MAPE$ and highest R^2, indicating superior accuracy in modelling skin impedance and drug flux. The existing BO algorithm was reliable but slower and less effective in highly non-convex spaces such as stratified skin models. Moreover, the PSO algorithm offered faster convergence but often failed in local minima due to its basic velocity-position update rule. The GA provided a good balance of exploration and exploitation, yet showed slower convergence compared to EOA. This analysis demonstrates that the proposed EOA offers the best trade-off between speed, accuracy, and robustness, making it ideal for complex biomedical optimisation tasks.

Table 8 presents a comparison of state-of-the-art models with the proposed model in terms of efficiency and computational criteria. The proposed model achieves the highest accuracy (R^2 = 0.96) and the lowest error ($MAPE$ = 0.134), while maintaining a lower computational complexity of $O(n \log n)$. The use of EOA further enhances reliability by optimising circuit parameters and minimising parameter uncertainty across different body regions. Furthermore, the proposed model significantly reduces training and inference times compared to other models, which range from 180 to 300 s and 50 to 70 ms, respectively. Despite its complexity, the proposed model balances speed, accuracy, and efficiency for TDD. As a result, it is clearly shown that the proposed model is superior to traditional methods, making it ideal for real-time TDD applications.

Table 8. Comparison evaluation: State-of-the-art models vs the Proposed model.

Reference	R^2	$MAPE$	Complexity	Training time [s]	Inference time [ms]
[28]	0.81	0.492	$O(n^2)$	180	50
[29]	0.84	0.478	$O(n^2)$	240	60
[6]	0.76	0.529	$O(n^2)$	300	70
[8]	0.79	0.507	$O(n^2 \log n)$	220	65
Proposed	0.96	0.134	$O(n \log n)$	95	20

4. DISCUSSION

The simulation findings presented in the results section are supported by in-silico validation using established skin impedance datasets and numerical modelling techniques. Various anatomical and biophysical characteristics of the skin may influence prediction errors between regions, such as the palm and forearm. Due to its thick SC and high concentration of sweat glands, the palm retains higher drug concentrations, resulting in a lower $MAPE$ value. In contrast, the forearm, with its thinner skin, lower ionic concentrations, and greater moisture fluctuation, exhibits higher computational errors and less predictable impedance behaviour. These variations have a direct impact on drug diffusion and ion transport under iontophoretic stimulation. Additionally, EOA effectively reduces complexity while improving overall prediction accuracy by optimising region-specific circuit characteristics. Therefore, skin-specific features should be considered when optimising transdermal medication delivery techniques.

From this analysis, the proposed model is suitable for TDD applications due to its many benefits, including a low error rate ($MAPE$ = 0.134), high prediction accuracy (R^2 = 0.96), and low computational complexity ($O(n \log n)$). It efficiently optimises impedance parameters across different body parts and models skin stratification. The key advantage of the proposed method lies in its integration of multi-layer impedance modelling, ion flux simulation, and optimisation. However, its improved performance is countered by a slightly higher computational complexity. Moreover, the performance of the proposed model may be affected by variations in skin conditions, moisture, and temperature. Simulated data cannot accurately represent clinical circumstances in the current evaluation. To address these limitations, future work will focus on validating the model using clinical data from diverse populations and implementing it on embedded systems for real-time TDD applications.

5. CONCLUSION

This research presents a novel systematic approach to device-assisted TDD using an advanced skin impedance modelling method and optimisation techniques. The key original contributions and distinctions from previous work are summarised below:

- The SLRC model was developed by combining the Montague, CPE, and Tregear models to simulate multi-layer skin impedance more accurately.
- Compared to traditional models, the PBNP model provides accurate estimates of drug concentration and electrotransport flux across stratified skin layers with electric stimulation.
- EOA was used for the first time in TDD modelling to optimise impedance parameters, achieving lower computational error and faster convergence than the existing methods such as GA, PSO, and BO.
- The proposed model achieves the lowest $MAPE$ (0.134) and highest R^2 (0.96) compared to other existing models, demonstrating its robustness across various body regions.
- The results indicate that a frequency of 4×10^3 Hz yields the best impedance and drug penetration, highlighting the importance of frequency and current density in increasing drug levels.

Based on the experimental findings, the proposed model provides a robust and efficient framework for improving TDD systems, with promising implications for clinical applications. Future work includes in-vitro experiments using excised skin samples and in-vivo studies with biomedical research laboratories to validate and refine the model under physiological conditions. Additionally, we plan to explore other non-invasive enhancement techniques, such as ultrasound or microneedles with iontophoresis, to further optimise drug delivery efficiency and broaden the scope of TDD applications.

REFERENCES

[1] Dinu, M., Tatu, A. L., Cocoș, D. I., Nwabudike, L. C., Chirilov, A. M., Stefan, C. S., Earar, K., Dumitriu Buzia, O. D. (2024). Natural sources of therapeutic agents used in skin conditions. *Life*, 14 (4), 492. https://doi.org/10.3390/life14040492

[2] Nicze, M., Borówka, M., Dec, A., Niemiec, A., Bułdak, Ł., Okopień, B. (2024). The current and promising oral delivery methods for protein-and peptide-based drugs. *International Journal of Molecular Sciences*, 25 (2), 815. https://doi.org/10.3390/ijms25020815

[3] Heraudeau, M., Roux, C. M., Lahogue, C., Largilliere, S., Allouche, S., Lelong-Boulouard, V., Freret, T. (2023). Micropipette-guided Drug Administration (MDA) as a non-invasive chronic oral administration method in male rats. *Journal of Neuroscience Methods*, 398, 109951. https://doi.org/10.1016/j.jneumeth.2023.109951

[4] García, J., Ríos, I., Fonthal Rico, F. (2019). Design and analyses of a transdermal drug delivery device (TD^3). *Sensors*, 19 (23), 5090. https://doi.org/10.3390/s19235090

[5] Phatale, V., Vaiphei, K. K., Jha, S., Patil, D., Agrawal, M., Alexander, A. (2022). Overcoming skin barriers through advanced transdermal drug delivery approaches. *Journal of Controlled Release*, 351, 361-380. https://doi.org/10.1016/j.jconrel.2022.09.025

[6] Goyal, K., Borkholder, D. A., Day, S. W. (2022). Dependence of skin-electrode contact impedance on material and skin hydration. *Sensors*, 2 (21), 8510. https://doi.org/10.3390/s22218510

[7] Ordiz, I., Vega, J. A., Martín-Sanz, R., García-Suárez, O., del Valle, M. E., Feito, J. (2021). Transdermal drug delivery in the pig skin. *Pharmaceutics*, 13 (12), 2016. https://doi.org/10.3390/pharmaceutics13122016

[8] Murphy, B. B., Scheid, B. H., Hendricks, Q., Apollo, N. V., Litt, B., Vitale, F. (2021). Time evolution of the skin–electrode interface impedance under different skin treatments. *Sensors*, 21 (15), 5210. https://doi.org/10.3390/s21155210

[9] Wang, Y., Zeng, L., Song, W., Liu, J. (2022). Influencing factors and drug application of iontophoresis in transdermal drug delivery: An overview of recent progress. *Drug Delivery and Translational Research*, 12, 15-26. https://doi.org/10.1007/s13346-021-00898-6

[10] Bok, M., Kwon, Y. I., Huang, Z. M., Lim, E. (2023). Portable iontophoresis device for efficient drug delivery. *Bioengineering*, 10 (1), 88. https://doi.org/10.3390/bioengineering10010088

[11] Li, Y., Yang, J., Zheng, Y., Ye, R., Liu, B., Huang, Y., Zhou, W., Jiang, L. (2021). Iontophoresis-driven porous microneedle array patch for active transdermal drug delivery. *Acta Biomaterialia*, 121, 349-358. https://doi.org/10.1016/j.actbio.2020.12.023

[12] Liu, L., Zhao, W., Ma, Q., Gao, Y., Wang, W., Zhang, X., Dong, Y., Zhang, T., Liang, Y., Han, S., Cao, J., Wang, X., Sun, W., Ma, H., Sun, Y. (2023). Functional nano-systems for transdermal drug delivery and skin therapy. *Nanoscale Advances*, 5 (6), 1527-1558. https://doi.org/10.1039/D2NA00530A

[13] Khan, S. U., Ullah, M., Saeed, S., Saleh, E. A. M., Kassem, A. F., Arbi, F. M., Wahab, A., Rehman, M., ur Rehman, K., Khan, D., Zaman, U., Khan, K. A., Khan, M. A., Lu, K. (2024). Nanotherapeutic approaches for transdermal drug delivery systems and their biomedical applications. *European Polymer Journal*, 207, 112819. https://doi.org/10.1016/j.eurpolymj.2024.112819

[14] Rinaldi, A. O., Korsfeldt, A., Ward, S., Burla, D., Dreher, A., Gautschi, M., Stolpe, B., Tan, G., Bersuch, E., Melin, D., Lord, N. A., Grant, S., Svedenhag, P., Tsekova, K., Schmid-Grendelmeier, P., Möhrenschlager, M., Renner, E. D., Akdis, C. A. (2021). Electrical impedance spectroscopy for the characterization of skin barrier in atopic dermatitis. *Allergy*, 76 (10), 3066-3079. https://doi.org/10.1111/all.14842

[15] Fortune, B. C., Pretty, C. G., Cameron, C. J., McKenzie, L. R., Chatfield, L. T., Hayes, M. P. (2021). Electrode–skin impedance imbalance measured in the frequency domain. *Biomedical Signal Processing and Control*, 63, 102202. https://doi.org/10.1016/j.bspc.2020.102202

[16] Qiao, Z., Xu, Z., Yin, Q., Zhou, S. (2023). Structure-preserving numerical method for Maxwell-Ampère Nernst-Planck model. *Journal of Computational Physics,* 475, 111845. https://doi.org/10.1016/j.jcp.2022.111845

[17] Rosseto, M. P., Evangelista, L. R., Lenzi, E. K., Zola, R. S., Ribeiro de Almeida, R. R. (2022). Frequency-dependent dielectric permittivity in Poisson–Nernst–Planck model. *The Journal of Physical Chemistry B*, 126 (34), 6446-6453. https://doi.org/10.1021/acs.jpcb.2c03663

[18] Ehtiati, K., Eiler, J., Bochynska, A., Nissen, L. L., Strøbech, E., Nielsen, L. F., Thormann, E. (2023). Skin and artificial skin models in electrical sensing applications. *ACS Applied Bio Materials*, 6 (8), 3033-3051. https://doi.org/10.1021/acsabm.3c00356

[19] Bora, D. J., Dasgupta, R. (2020). Sensitivity of montague model of skin for predicting physiological variation in skin layers. In *2020 International Conference on Contemporary Computing and Applications (IC3A)*. IEEE, 13-16. https://doi.org/10.1109/IC3A48958.2020.233260

[20] Bora, D. J., Dasgupta, R. (2020). Estimation of skin impedance models with experimental data and a proposed model for human skin impedance. *IET Systems Biology*, 14 (5), 230-240. https://doi.org/10.1049/iet-syb.2020.0049

[21] Ghoneim, M. S., Mohammaden, A., Said, L. A., Madian, A. H., Radwan, A. G., Eltawil, A. M. (2021). A comparative study of different human skin impedance models. In *2021 38th National Radio Science Conference (NRSC)*. IEEE, 271-277. https://doi.org/10.1109/NRSC52299.2021.9509823

[22] Holm, S., Holm, T., Martinsen, Ø. G. (2021). Simple circuit equivalents for the constant phase element. *PloS One*, 16 (3), e0248786. https://doi.org/10.1371/journal.pone.0248786

[23] Bora, D. J. (2023). A study of the characteristics of Skin Impedance Models based on the simulation of models. In *2023 IEEE 8th International Conference for Convergence in Technology (I2CT)*. IEEE. https://doi.org/10.1109/I2CT57861.2023.10126190

[24] Oyelade, O. N., Ezugwu, A. E.-S., Mohamed, T. I. A., Abualigah, L. (2022). Ebola optimization search algorithm: A new nature-inspired metaheuristic optimization algorithm. *IEEE Access*, 10, 16150-16177. https://doi.org/10.1109/ACCESS.2022.3147821

[25] Kwon, I., Kwak, D. Y., Jo, G. (2021). Discontinuous bubble immersed finite element method for Poisson–Boltzmann–Nernst–Planck model. *Journal of Computational Physics*, 438, 110370. https://doi.org/10.1016/j.jcp.2021.110370

[26] Xie, Y., He, J., Li, S., Chen, X., Zhang, T., Zhao, Y., Lin, Y., Cai, X. (2023). A transdermal drug delivery system based on nucleic acid nanomaterials for skin photodamage treatment. *Advanced Functional Materials*, 33 (46), 2303580. https://doi.org/10.1002/adfm.202303580

[27] Limcharoen, B., Wanichwecharungruang, S., Banlunara, W., Darvin, M. E. (2025). Seeing through the skin: Optical methods for visualizing transdermal drug delivery with microneedles. *Advanced Drug Delivery Reviews*, 217, 115478. https://doi.org/10.1016/j.addr.2024.115478

[28] Massot, B., Desmazure, E., Montalibet, A., McAdams, E., Gehin, C. (2024). A portable device performing continuous impedance spectroscopy for skin conductivity. *IEEE Sensors Journal*, 24 (24), 41125-41135. https://doi.org/10.1109/JSEN.2024.3485187

[29] Rowe, D., Rowe, M. (2024). Characterising skin electrical impedance using tape stripping methods: A bioelectrical study of a porcine model. *Cureus*, 16 (8), e66566. https://doi.org/10.7759/cureus.66566

Received March 12, 2025
Accepted July 25, 2025